A Novel Volumetric Feature Extraction Technique with Applications to MR Images

Edward A. Ashton,* Kevin J. Parker, *Fellow, IEEE*, Michel J. Berg, and Chang Wen Chen

Abstract— A semiautomated feature extraction algorithm is presented for the extraction and measurement of the hippocampus from volumetric magnetic resonance imaging (MRI) head scans. This algorithm makes use of elements of both deformable model and region growing techniques and allows incorporation of *a priori* operator knowledge of hippocampal location and shape. Experimental results indicate that the algorithm is able to estimate hippocampal volume and asymmetry with an accuracy which approaches that of laborious manual outlining techniques.

Index Terms— Deformable model, feature extraction, MRI, three-dimensional.

I. INTRODUCTION

MANY anatomical feature extraction algorithms have been proposed recently which make use of either the two-dimensional (2-D) active contour model of Kass *et al.* (*snakes*) [1]–[5] or one of several three-dimensional (3-D) extensions, which are frequently referred to as either *blobs, balloons,* [6]–[9] or *deformable templates* [10], [11]. These approaches have a common origin, and as a result they share certain common difficulties. The 2-D techniques frequently have difficulty tracking between slices, particularly if the major axis of the desired structure is not perpendicular to the imaging plane. Additionally, they are generally based on edge detection and are prone to locking onto spurious edges, requiring manual adjustment. One primary difficulty of these 3-D algorithms can be understood intuitively. A "snake" is a string of pixels, with each pixel interacting directly with its neighbors, while a deformable surface model requires a mesh of voxels, with a corresponding increase in number of elements and number of interactions of each element.

Clearly, it is possible for the computational complexity of this model to increase very rapidly. Finite element techniques, therefore, are used to reduce computation time. If large elements are used, details of the structure being extracted are lost. If small elements are used, computation time may extend into hours or days. The model described in this paper requires no such tradeoff between resolution and computational intensity. More importantly, snake-based techniques do not incorporate any *a priori* model of the expected shape and size of the structure of interest. Therefore, they may not be useful for the identification of structures whose boundaries may be indistinct, such as the hippocampus, a gray-matter structure of the human brain, which is adjacent to other gray matter structures and has no distinguishable boundary along a significant portion of its surface. Our algorithm begins with a simply initialized shape model, composed of the superposition of multiple appropriately placed and shaped ovoids. This *a priori* modeling allows our algorithm to fill in areas of the surface of the structure of interest which have no apparent boundary in the data.

We propose a deformable model technique which incorporates some of the same goals as the region growing technique, which has been presented by Taylor and Barrett [12]. The Taylor algorithm provides competitive region growth from one or more seeds through comparison of border voxels to the first-order statistics of voxels which have already been absorbed. Our algorithm combines this concept with the idea of the deformable model. We begin with one or more seed voxels. Each of these seeds will, if left unconstrained, expand into an ovoid with a predetermined volume and preset ratios between radii in the x, y, and z directions. Constraining forces are elastic surface tension, deviation from the expected surface normal, and resistance from surrounding tissue. The expansive force is provided by internal pressure, which is gradually increased until either the expected volume is reached or no further expansion is possible due to constraining tissue.

One important application of this algorithm is in the quick and accurate *in vivo* volume measurement of the hippocampus and amygdala. Jack *et al.* and others [13], [14] have shown that such a measurement may be an important aid in the diagnosis of intractable temporal lobe epilepsy. Jack *et al.* [15] and Kesslak *et al.* [16] have also shown that this data may predict dementia of the Alzheimer type. Current techniques for obtaining these volumes include manual tracing, thresholding, and random marking. These processes require extensive human interaction, and are time consuming and subject to variation.

In this paper, our algorithm is tested for robustness and stability under a wide range of conditions. The results of our algorithm's identification of a phantom structure within a series of simulated magnetic resonance imaging (MRI) scans are tested against known correct results. We also compare our algorithm's performance in identifying the hippocampus on an

*E. A. Ashton is with the Optical Sciences Division, Naval Research Laboratory, 4555 Overlook Ave. SW, Washington, DC 20375 USA (e-mail: ashton@dynasun. nrl.navy.mil).

K. J. Parker and C. W. Chen are with the Department of Electrical Engineering, University of Rochester, Rochester, NY 14627 USA.

M. J. Berg is with the Department of Neurology, University of Rochester, Rochester, NY 14627 USA.

actual series of MRI brain scans against a physician's manual identifications.

II. MODELING

The following deformable model algorithm is designed to operate on data which has previously been segmented by tissue type. An algorithm to provide such a segmentation for MR images has been presented previously in [2]. An algorithm for the segmentation of ultrasound images has been presented in [17].

As has been implied in Section I, this deformable model algorithm is essentially a region-growing technique, with added morphological constraints which come into play only under certain conditions. The physical system modeled is an expanding bubble with a preset geometry. The final volume of the model is limited by the ratio between internal pressure and elastic surface tension. Local surface morphology is controlled by the constraining force of surrounding tissue and by a penalty for deviation from the expected surface normal.

More precisely, the expansive force at a given boundary voxel is

$$F = p - (S + N + C) \tag{1}$$

where p is internal pressure, given by

$$p = nRT/V \tag{2}$$

in which R is the universal gas constant, V is the current volume of the model, T is temperature, held constant at $1/R$, and n is set at the value necessary to reach force equilibrium at the expected final volume and surface area—i.e., the volume and surface area which the model would reach if it were allowed to grow unconstrained. This volume and area are calculated based upon an *a priori* shape model, the derivation of which will be discussed in the Section III. S in (1) is surface tension, which is proportional to the total surface area of the model. N is deviation from expected surface normal, given by

$$N = c_N \cos^{-1}(r_e \cdot r_a/(|r_e||r_a|)) \tag{3}$$

where c_N is a weighting constant, r_e is the surface normal expected given a purely ovoid expansion, and r_a is the actual local surface normal. Finally, C is the constraining force of the surrounding tissue. If this force is nonzero and is overcome, the stiffness value associated with that voxel is distributed among all neighboring voxels with nonzero stiffness. This allows tissue to "give" a few voxels to the expanding volume before stiffening and holding, which provides morphological smoothing in three dimensions. In all experiments described in this work, and in most cases, the evaluation of C will be a binary decision. If the border voxel is of the same tissue type as the structure of interest, $C = 0$, otherwise C will be very large. In other words, the model is forbidden to expand into foreign tissue. However, if morphological smoothing is desired or the segmentation is not trusted, C may be evaluated as a linear or hyperbolic function of the absolute difference between the tissue type of interest and the type of the border voxel.

It is the final energy term, N, which gives the model much of its flexibility. It is this term, which has a function similar to that of the β term in the original *snake* formulation [1],
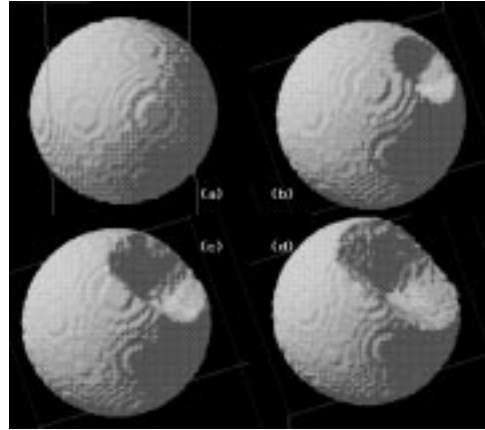

Fig. 1. (a) Sphere grown from a single seed voxel in the presence of a constraining point with $c_N = 0$. The model grows around the point and absorbs it. (b) $c_N = 25$. A deep, steep-sided crater is created by the constraining point. (c) $c_N = 50$. A wider crater is created. (d) $c_N = 75$. There is very little flexibility in the surface of the model.

which allows us to do without the finite element techniques which are most often employed for 3-D modeling. It allows fine control over the final morphological characteristics of the model, while enforcing the smoothness in three dimensions that we expect to see in biological structures. Its functioning is demonstrated in Fig. 1. In this experiment an ovoid is grown from a single seed voxel in the presence of a small, hard point of constraining tissue, while the relative weighting of the N term is allowed to vary. Note that the effect is similar to what one would expect to observe in a physical system if the model were given stiffer or softer skin.

A flowchart for the operation of this algorithm is given in Fig. 2.

III. FEATURE EXTRACTION

The extraction of structures from volume data sets using this model is fairly straightforward. One or more seeds are planted by an operator at or near the center of the structure which is to be extracted. These seeds then grow until they either encounter tissue walls or reach their growth potential, and form smooth boundaries where none are apparent in the data. The most interesting problem in this case concerns initialization. How many seeds are planted, and where, and how is the growth potential of each seed determined? The answers to these questions will depend upon the geometry of the structure of interest, which will determine the complexity of the required *a priori* shape model. An ovoid or near-ovoid shape, such as the interior of a heart chamber, may be sufficiently modeled by a single seed. A structure with a complex shape in only one viewing plane will require a string of seeds in that plane with appropriately adjusted growth potentials. A structure with a complex shape in two or more viewing planes, such as the hippocampus, will require a string of seeds which may be entirely nonplanar.

One possible way to obtain such an initial model is to make use of data from an anatomic atlas, as is done for 2-D models in [18], and for 3-D models in [11]. However, in this case registration is a nontrivial problem. Additionally, abnormal
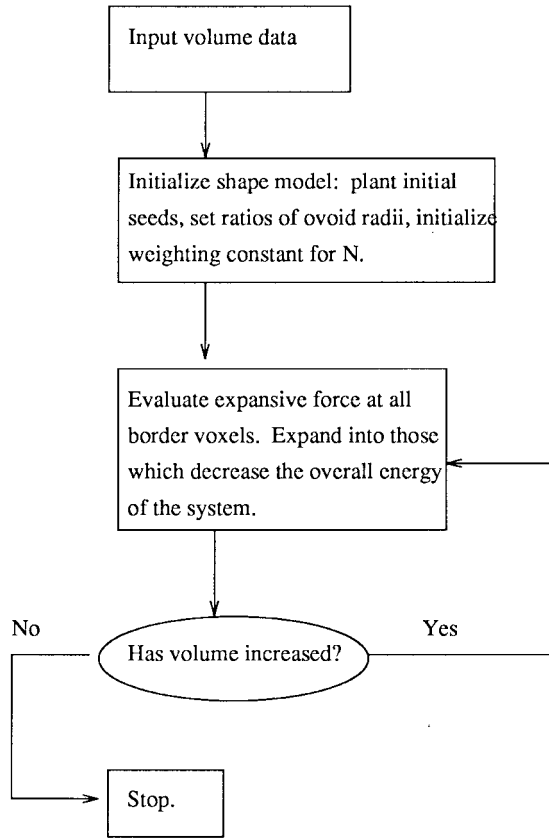
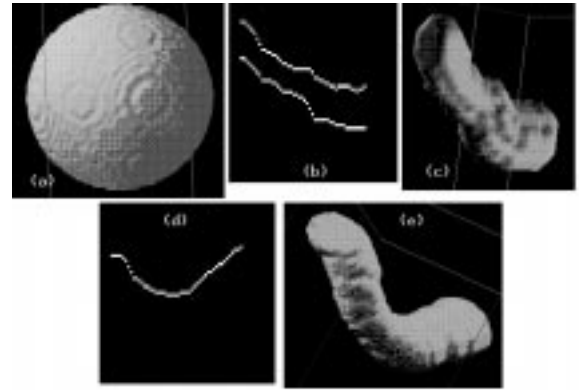Fig. 2.   Flowchart for feature extraction using the bubble algorithm.

Fig. 3.   (a) Solid model resulting from a single unconstrained seed voxel. (b) Initialization contour. Seed voxels are laid along the center line of the contour. (c) Solid model resulting from the unconstrained growth of seeds resulting from (b). (d) Z-plane curve, which adjusts the placement of the seeds resulting from (b). (e) Solid model resulting from the combination of the initialization curve shown in (b) with the z-plane curve shown in (d).

cases (which are, after all, the ones that are of the most interest) may vary widely from the averages found in an atlas, causing errors in the extraction process. A simpler and potentially more accurate solution is to provide an initial contour on one slice, as in [2]. The algorithm then:

- identifies the long axis of this contour;
- lays a line of seeds along its center line;
- calculates the growth potential of each seed from the width of the initial contour at that point.

If out of plane curvature is required, a single line curve in an orthogonal plane may be provided. Fig. 3(a) shows an ovoid grown in free space from a single seed voxel. Fig. 3(b) shows a single plane contour such as is described in the second case above. The resultant solid model is given in Fig. 3(c). An orthogonal plane curve, as described in Case 3, is given in Fig. 3(d). The solid model which results when this curve is combined with the initialization contour in Fig. 3(b) is shown in Fig. 3(e).

There are a number of concerns which are relevant to this approach. First is that the "center slice" of the feature which is to be extracted may not be precisely known. Because this model assumes a certain amount of symmetry, an error in centering may produce an error in the result. This error will be quantified in Section IV. Furthermore, the assumption of symmetry in two or three dimensions in Case 2 or Case 1, respectively, makes it necessary to carefully choose the optimal initialization plane. This plane should be oriented such that the symmetry of the model most accurately reflects

the symmetry of the feature in question. If the feature is a reasonably symmetrical one, such as a chamber of the heart, this may not be difficult. However, in the case of features which are very irregularly shaped, such as the hippocampus, initial orientation is a serious concern.

Another concern is the selection of parameters. The two relevant parameters in this case are c_N, which helps determine the final surface morphology of the extracted feature, as illustrated in Fig. 1, and the selected ratio between the y and z radii of the *a priori* model. If the approximate size and shape of the target feature is known to the operator, the latter term may be easily estimated. Furthermore, if the boundaries in the z direction are fairly well defined in the segmented data, over-estimation of this parameter will not lead to any error in the resultant feature extraction. Selection of c_N is somewhat more difficult. There is no way to algorithmically optimize this term. Optimization must be carried out experimentally. However, experimental experience with this algorithm, as well as experience with other deformable model techniques [2], indicates that this term may be optimized a single time for application to a broad class of image sequences. The experimental optimization of c_N is described in Section IV. All subsequent experiments in this work were carried out using $c_N = 70$.

IV. EXPERIMENTAL PROCEDURE AND DISCUSSION

A. Demonstration of Concept

Our experiments have included testing this technique on a 3-D MRI phantom which mimics the statistics and morphology of the hippocampal region of the MRI head scan used in later experiments, as well as on an actual multiple-slice MRI head scan. The application in this case is the extraction and reconstruction of the hippocampus, a gray-matter structure of the human brain whose volume and morphology are useful in the detection and prediction of a number of neurological disorders, including intractable temporal lobe epilepsy, and dementia of the Alzheimer's type [14], [15]. In the phantom
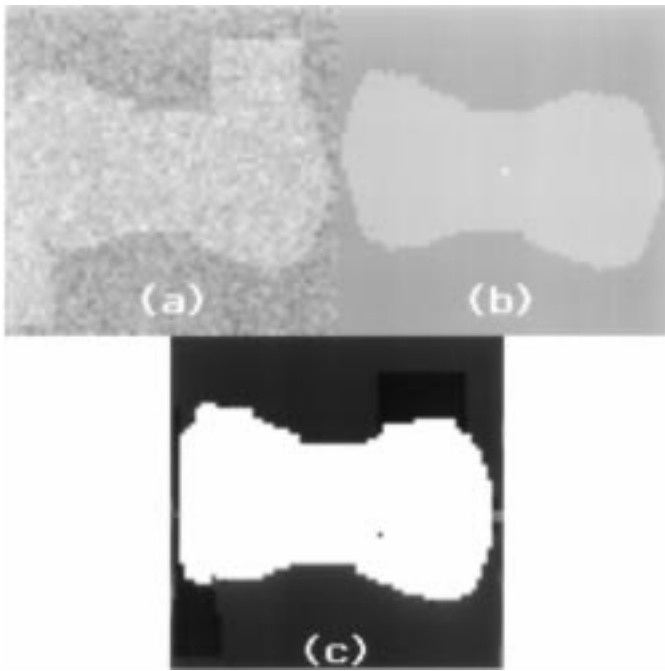
Fig. 4. (a) Center slice from the MRI phantom. (b) Ideal segmentation and extraction of simulated hippocampus from the center slice of the MRI phantom. (c) Extraction of the simulated hippocampus from this slice as calculated by our algorithm.

experiments, the experimental results were compared to the original known phantom structure. In the clinical data set, a physician's manual identifications were used as a point of comparison. The algorithm was tested for subjective visual accuracy, as well as for accuracy in volume measurement and voxel classification.

The center slice of the MRI phantom used in our initial experiments is given in Fig. 4(a). The phantom has a background graylevel of 155 and a foreground graylevel of 190 and is corrupted by spatially invariant Gaussian noise with $\sigma = 15.0$. An ideal segmentation and extraction of the simulated hippocampus is given in Fig. 4(b). Note that ideal extraction involves separation of the structure both from statistically dissimilar and statistically identical regions. The extraction from this slice as calculated by our algorithm is given in Fig. 4(c). Volume renderings of the original phantom (grayscale segmented), the ideally extracted feature, and the feature as reconstructed by our algorithm are given in Fig. 5(a)–(c). The percent of misclassified voxels, defined here as 100* [number misclassified/correct volume], is 5.50%. The error in calculated volume is 3.38%.

As was mentioned in Section III, the initialization technique used here is partially based on knowledge of the center of the feature of interest. It is important, therefore, to test the robustness of the algorithm with regard to errors in the estimation of that center. For this series of experiments we made use of the MRI phantom described in the previous paragraph. Repeated trials were conducted in which the initialization of the model was moved progressively farther off center. Error was found to remain fairly constant to an offset of ten voxels, after which it increased exponentially. Note that the overall width of the feature was 46 voxels. The group of slices on
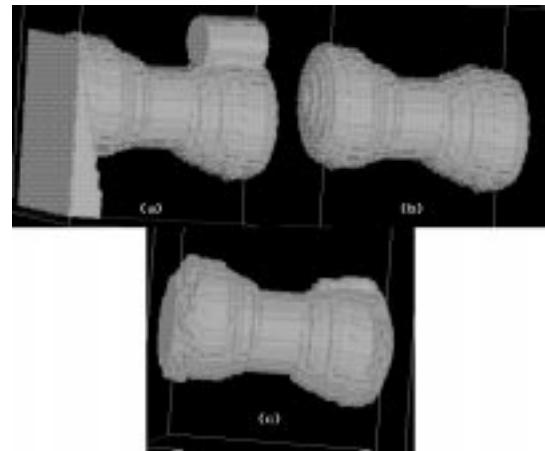

Fig. 5. (a) The original MRI phantom, segmented and volume rendered. (b) Volume rendering of the ideal segmentation and extraction of the simulated hippocampus. (c) Volume rendering of the simulated hippocampus as calculated by our algorithm.
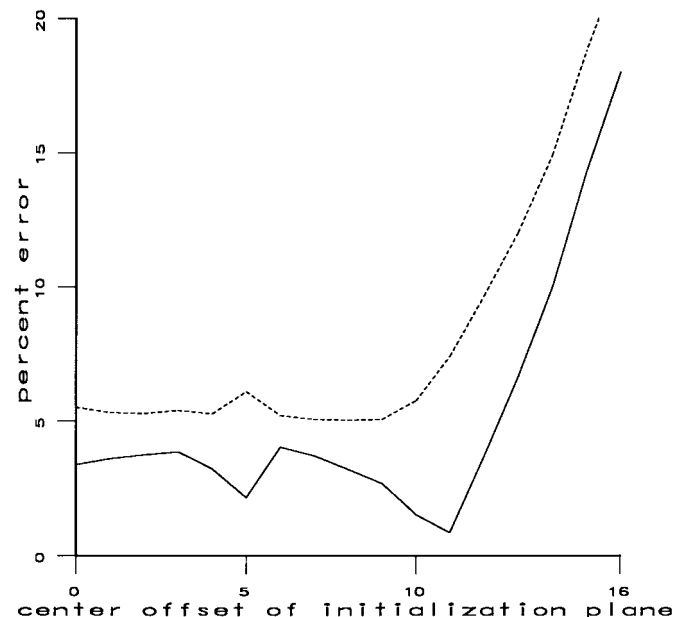

Fig. 6. Results of the center-offset trials. The solid line indicates error in volume estimation. The dashed line indicates error in voxel classification. Note that error remains relatively constant until ten voxels offset—a band of stability which covers 43% of the structure of interest.

which the model could be initialized while achieving fairly consistent results, therefore, amounts to 43% of the total slices containing portions of the structure. We feel that this indicates considerable robustness in the algorithm. A plot of percent voxel error and error in volume estimation versus center offset for all trials is shown in Fig. 6.

Our second set of experiments was concerned with determining the model's sensitivity and stability with respect to the parameter c_N, the weighting constant for the deviation from expected surface normal energy term. These experiments also made use of the phantom described above. Using an optimally centered initialization, we allowed c_N to vary from 0 to 150. Error was calculated in terms of both volume estimation and percentage of misclassified voxels. In both cases maximum error was found at $c_N = 0$. This is as expected, since in this
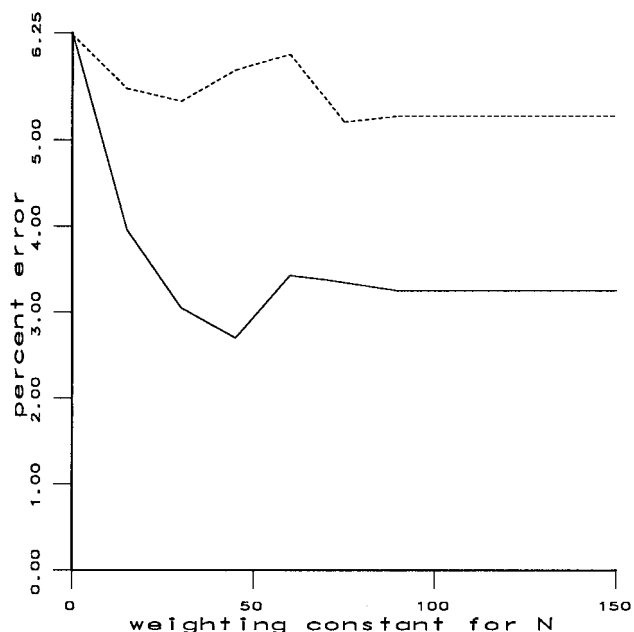
Fig. 7. Results of the c_N trials. The solid line indicates error in voxel classification. The dashed line indicates error in volume estimation. Note that the error is maximum at $c_N = 0$ and that a region of stability appears in both error measures at values of c_N greater than 90.
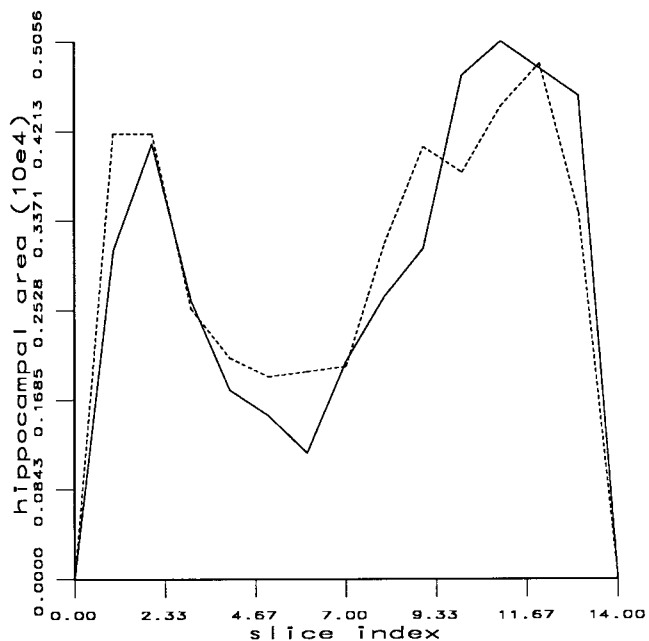
Fig. 8. Comparison of manual (dashed line) to calculated hippocampal (automated: solid line) areas for a 13-slice section of a 60-slice MRI head study. Deviation in total volume calculation was 3.26%.

Fig. 9. (a) Hippocampal region of slice 6 from our MRI head study. (b) Automatic identification of the hippocampus. Note that the "tail" to the left of the circumscribed volume has not been included in the identification. (c) Manual identification of the hippocampus. Note that the shape has been oversimplified and that the area of the "tail" has been overestimated.

case the N term is ignored and there is no control of surface morphology. A minimum was found in percent voxel error at $c_N = 60$ and in volume estimation at $c_N = 45$. A stable region with slightly higher error was found in both error measures beginning at $c_N = 90$. A plot of percent voxel error and error in volume estimation versus c_N for all trials is given in Fig. 7.

Taken together, these two sets of experiments demonstrate a high level of robustness and stability in this algorithm. Because there is no algorithmic method for determining an optimal c_N, a high level of sensitivity to this parameter (which would
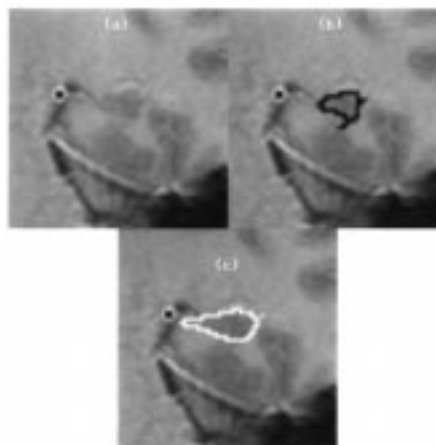
indicate a need for reoptimization for each new application) would be a very serious drawback. Because near-optimal results are obtained in the very large stable region of $c_N > 90$, no such optimization appears to be necessary.

We next wished to examine the applicability of this algorithm to actual data. To that end, our next experiment was conducted on a 13-slice section of a 60-slice coronal spoiled grass (SPGR) MRI head sequence with 35/5/30/2 (repetition time/echo time/flip angle/excitations). Slice thickness was 3.0 mm. Imaging was performed using a General Electric Signa 1.5-T superconducting system (Milwaukee, WI). Manual identifications of the hippocampus were made on each of the slices by a physician. The slices were then grayscale segmented, using the technique described in [2], and replicated (reproduced three times) to form nearly cubic voxels. Because the pixel size on these images was 0.7 mm, this required replication by a factor of four. The volume was then rotated to obtain a sagittal view. An initialization contour was provided for the center slice of this volume, and the algorithm was allowed to run with $c_N = 90$. A 3-D reconstruction was produced from the result. The volume was then rotated back to a coronal orientation and reduced in size to the original resolution for comparison to the manual identifications.

As has been previously noted, one important application of this algorithm is the *in vivo* volume measurement of the hippocampus. For this reason, we first compared the calculated area of the hippocampus on each slice of the scan to the area of the manual identifications. A plot of this comparison is given in Fig. 8. Close correlation between manual and automatic area calculation is found on nearly every slice. Additionally, an examination of the slices where large deviations exist shows that at least part of the error is in the *manual* identification. An example of this is slice 6; see Fig. 9. While the algorithm has clearly left off a portion of the "tail," to the left of the outlined structure, it is also clear that the manual identification overestimates the area of that portion of the structure. Despite these errors, the total calculated hippocampal volume deviated from the manual volume by only 3.26%. Note that Jack [13]
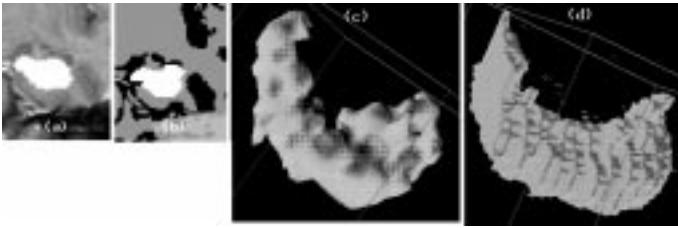
Fig. 10. (a) Physician's manual identification of the hippocampus on one slice of a coronal volumetric MRI head scan. (b) Hippocampus as identified by our algorithm on that same slice. (c) Volume-rendered reconstruction of the right hippocampus as identified by our algorithm. (d) Volume-rendered reconstruction of the right hippocampus as identified manually.

has reported a coefficient of variation in manual identification of the volume of the hippocampus by expert users of 1.9%. The percentage of differently classified voxels between these two volumes was 4.35%.

The hippocampal region of slice 9 of 13 from our MRI head scan is given in Fig. 10(a). The physician's manual identification of the hippocampus is shown in white. Fig. 10(b) shows our algorithm's identification of the hippocampus on that same slice. A volume-rendered reconstruction of the automatically identified full hippocampus is given in Fig. 10(c). The corresponding manual reconstruction is given in Fig. 10(d). Examination of the reconstructions shows some of the possible advantages this algorithm may have over manual segmentation, other than a saving of man-hours. The automatic reconstruction has a smooth and continuous surface, as one might expect from a natural structure, while the manual reconstruction is blocky and clearly truncated at the end planes. Additionally, there are discontinuities in the surface of the manual reconstruction, which are a result of the physician having only one slice of data available at a time, while our algorithm has access to the entire volume as a whole. These observations indicate that some of the difference between the manual and automatic segmentations may in fact be due to error in the manual outlining, rather than to error produced by our algorithm.

B. Application to MR Clinical Study

As has been previously stated, it is known that numerous chronic conditions such as normal aging [19], Alzheimer's disease [16], autism [20], and schizophrenia [21], are associated with anatomic changes within the brain that can be detected with quantitative measures of various structures on MRI studies of the head in populations of patients. In certain disorders, pathologic changes occur to a significant enough degree that they can be detected within the individual patient. For example, in temporal-lobe epilepsy, structural abnormalities within the hippocampi can be detected with MRI [13]. Unilateral or asymmetric atrophy of the hippocampi, identified on MRI, correlates with hippocampal sclerosis, location of seizure onset, and outcome after epilepsy surgery (temporal lobectomy) [15], [22].

In all of these studies, the assessment of brain structures on the MRI was done by manual outlining of the structure of interest. This is a time consuming, labor intensive process that is subject to intraobserver and interobserver measurement

errors. The extensive labor requirements for manual measurements has resulted in the almost exclusive use of visual (qualitative) analysis of brain structures in the clinical setting. In many cases, this likely results in lost information. In order to implement routine quantitative analysis of MRI (and other medical imaging modalities), automated systems need to be developed. It is with this end in mind that the algorithm presented in the previous section was developed.

The bubble algorithm has been validated under realistic circumstances previously in [23]. However, in order to test the algorithm in a clinical environment, a study was conducted using patients with temporal-lobe epilepsy who were poorly responsive to appropriate antiseizure medications. These patient all underwent evaluation for epilepsy surgery. MRI is a primary study performed in this preoperative evaluation, because it can detect hippocampal sclerosis (gliosis and neuronal cell loss). Hippocampal sclerosis is the hallmark feature of temporal-lobe epilepsy. Surgical removal of a sclerotic hippocampus and adjacent structures eliminates seizures in many patients with medically intractable temporal-lobe epilepsy. The results of manual outlining of the hippocampus were compared to the results of the bubble algorithm on the preoperative MRI. These results were correlated to side of seizure onset.

MRI was performed using a 1.5-T superconducting system. A volume study consisted of a SPGR sequence with 35/5/30/2 (repetition time/echo time/flip angle/excitations). The sections were 256×256 pixels with a field of view of 16-cm square and a slice thickness of 1.5 mm.

Nine patients, five with right-temporal-lobe epilepsy and four with left-temporal-lobe epilepsy, were selected randomly from those with an adequate-quality MRI study from the University of Rochester Comprehensive Epilepsy Program archives.

All raters were blind to patient information and results of the other method at the time of the rating. Manual outlining was performed by a trained neurologist on a SUN SPARC 5 workstation. The bubble algorithm was initialized by a nonmedical operator with a cursory knowledge of the location and structure of the hippocampus.

The results of this experiment are given in Table I. The statistic of interest in this case is the percentage difference in volume from left to right hippocampus (i.e., the degree of asymmetry.) The manually outlined results showed three patients with atrophic right hippocampi and six patients with atrophic left hippocampi. The automatically identified results show five with atrophic right hippocampi and four with atrophic left hippocampi. Note that the side in which the seizures are known to occur is expected to be atrophic. A scatterplot of automated results versus manual results is given in Fig. 11.

The average error between manual and automated asymmetry measures was 0.016. The standard deviation of the error distribution was 0.065. These figures show good agreement between the manual and automated identification of asymmetry. The identification of the side of atrophy was identical in seven of the nine cases, with the two cases of disagreement both having asymmetry of less than 7%. Interestingly enough, in the two cases in which the automated and manual identification

TABLE I
SUMMARY OF RESULTS FROM CLINICAL TRIALS

Patient No.	Epilepsy Side	Automated $(R-L)/(R+L)$	Manual $(R-L)/(R+L)$	Error	Auto. Vol R	Auto Vol L	Man. Vol. R	Man. Vol. L
2	Right	−.003	−.003	−.003	5.172 cc	5.203 cc	4.991 cc	5.367 cc
7	Left	.383	.281	−.101	4.003 cc	1.786 cc	3.661 cc	2.055 cc
10	Left	.186	.257	.070	4.231 cc	2.904 cc	4.866 cc	2.882 cc
12	Right	−.065	.022	.088	4.129 cc	4.703 cc	4.601 cc	4.403 cc
14	Right	.315	−.344	−.029	2.371 cc	4.552 cc	2.397 cc	4.901 cc
15	Left	.061	.138	.078	4.482 cc	3.966 cc	4.719 cc	3.574 cc
17	Right	−.023	−.016	.007	3.931 cc	4.116 cc	4.121 cc	4.254 cc
18	Right	−.004	.068	.073	5.531 cc	5.580 cc	5.749 cc	5.012 cc
19	Left	.354	.343	−.011	3.595 cc	1.715 cc	3.484 cc	1.704 cc

Note that a negative number in $(R-L)/(R+L)$ indicates right hippocampal atrophy, while a positive number in this column indicates left hippocampal atrophy.
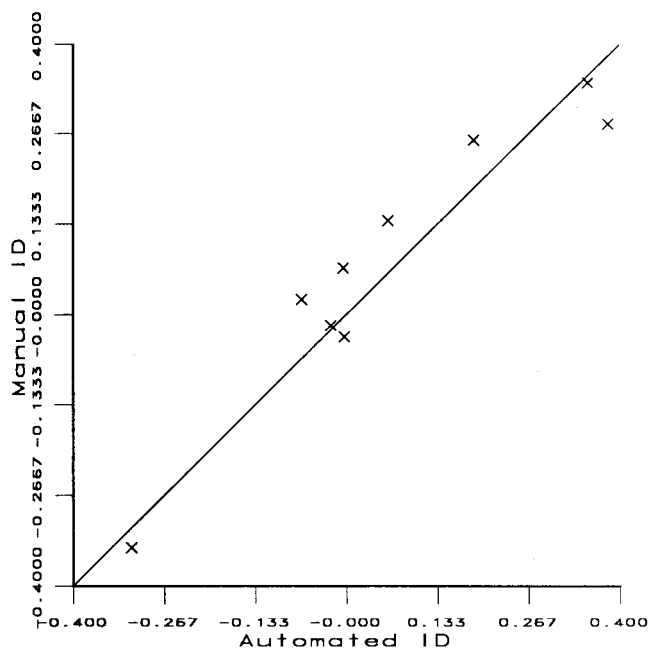

Fig. 11. Scatterplot of automated versus manual measures of asymmetry.

of atrophy disagree, the known origin of seizures is consistent with the results of the automated identification.

This study, while clearly limited in scope, demonstrates the utility of the algorithm described in this paper in a clinical setting. The bubble algorithm is clearly able to identify asymmetry in the hippocampi with an accuracy that surpasses the visual examination which is current clinical practice, and may approach in accuracy, manual outlining of the hippocampus on each slice. Finally, it should be noted that even greater accuracy could most likely be achieved in the automated identifications by an operator with a more thorough knowledge of neurological anatomy.

REFERENCES

[1] M. Kass, A. Witkin, and D. Terzopolous, "Snakes: Active contour models," *Int. J. Comput. Vis.*, pp. 321–331, 1988.
[2] E. Ashton, M. Berg, K. Parker, C. W. Chen, J. Weisberg, and L. Ketonen, "Segmentation and feature extraction techniques, with applications to MRI head studies," *Magn. Reson. Med.*, vol. 33, pp. 670–677, 1995.
[3] R. P. Grzeszczuk and D. N. Levin, "Brownian strings: Segmenting images with stochastically deformable contours," in *Visualization in Biomedical Computing*. Rochester, MN, Oct. 1994, pp. 72–89.
[4] I. Carlbom, D. Terzopoulos, and K. Harris, "Computer assisted registration, segmentation, and 3-D reconstruction from images of neuronal tissue sections," *IEEE Trans. Med. Imag.*, vol. 13, pp. 351–362, June 1994.
[5] M. Demi, "New approach to automatic contour detection from image sequences: An application to ventriculographic images," *Comput, Biomed. Res.*, vol. 27, pp. 157–177, 1994.
[6] R. T. Whitaker, "Volumetric deformable models: Active blobs," in *Visualization in Biomedical Computing*. Rochester, MN, Oct. 1994, pp. 122–134.
[7] L. Cohen, "On active contour models and balloons," *CVGIP: Graphical Models Image Processing*, vol. 53, pp. 211–218, Mar. 1991.
[8] J. S. Liaw and B. H. McCormick, "Mapping biological structure by finite element analysis," in *Proc. 1st Conf. Visualization in Biomedical Computing*, 1990, pp. 352–359.
[9] Y. F. Wang and J.-F. Wang, "Surface reconstruction using deformable models with interior and boundary constraints," *IEEE Trans. Pattern Anal. Machine Intell.*, vol. 14, pp. 572–579, May 1992.
[10] J. W. Haller *et al.*, "Three-dimensional hippocampal MR morphometry with high-dimensional transformation of a neuroanatomic atlas," *Radiol.*, no. 202, pp. 787–791, 1997.
[11] J. W. Haller *et al.*, "Hippocampal MR imaging morphometry by means of general pattern matching," *Radiol.*, no. 199, pp. 787–791, 1996.
[12] D. C. Taylor and W. A. Barrett, "Image segmentation using globally optimum growth in three dimensions with an adaptive feature set," in *Visualization in Biomedical Computing*. Rochester, MN, Oct. 1994, pp. 98–107.
[13] C. R. Jack, F. W. Sharbrough *et al.*, "Temporal lobe seizures: Lateralization with MR volume measurements of the hippocampal formation," *Neuroradiol.*, vol. 175, pp. 423–429, 1990.
[14] F. Cendes, F. Andermann *et al.*, "MRI volumetric measurement of amygdala and hippocampus in temporal lobe epilepsy," *Neurol.*, vol. 43, pp. 719–725, 1993.
[15] C. R. Jack, R. C. Petersen *et al.*, "MR-based hippocampal volumetry in the diagnosis of Alzheimer's disease," *Neurol.*, vol. 42, pp. 183–188, 1992.
[16] J. Kesslak, O. Nalcioglu, and C. Cotman, "Quantification of magnetic resonance scans for hippocampal and parahippocampal atrophy in Alzheimer's disease," *Neurol.*, vol. 41, pp. 51–54, 1991.
[17] E. Ashton and K. J. Parker, "Multiple resolution Bayesian segmentation of ultrasound images," *Ultrason. Imag.*, vol. 17, pp. 291–304, 1995.
[18] T. F. Cootes, A. Hill, C. J. Taylor, and J. Haslam, "Use of active shape models for locating structures in medical images," *Image Vis. Computing*, vol. 12, no. 6, pp. 355–365, 1994.
[19] D. Murphy, C. DeCarli, M. Schapiro, S. Rapoport, and B. Horowitz, "Age-related differences in volumes of subcortical nuclei, brain matter, and cerebrospinal fluid in healthy men as measured with MRI," *Arch. Neurol.*, vol. 49, pp. 839–845, 1992.
[20] E. Courchesne, H. Townsend, and O. Saitoh, "The brain in infantile autism: Posterior fossa structures are abnormal," *Neurol.*, vol. 44, pp. 214–223, 1994.
[21] M. Shenton, R. Kikinis, and F. Jolesz, "Abnormalities of the left temporal lobe and thought disorder in schizophrenia; a quantitive MRI study," *New Eng. J. Med.*, no. 327, pp. 604–612, 1992.
[22] T. Lencz, G. McCarthy, and R. Bronen, "Hippocampus in temporal lobe epilepsy: Correlation of presurgical MRI volumetrics with postsurgical cell counts," *Epilepsia*, vol. 31, pp. 667–668, 1990.
[23] E. Ashton, K. J. Parker, and D. Phillips, "Automated extraction of the LV from 3d cardiac ultrasound scans," in *Proc. Visual Communication and Image Processing'96, SPIE*, Apr. 1996, vol. 2727–2741, pp. 423–429.